International Journal of Nanomedicine

Dovepress
open access to scientific and medical research

Open Access Full Text Article

ORIGINAL RESEARCH

A pH-Sensitive Nanoparticle as Reactive Oxygen Species Amplifier to Regulate Tumor Microenvironment and Potentiate Tumor Radiotherapy

Xiaomei Jiang[1,*], Xiaohong Jiang[2,*], Dongjie Wu[1], Wanzhu Xie[3], Xiong Liu[1], Jintao Zheng[4]

[1]Department of Dermatology, Liuzhou Traditional Chinese Medicine Hospital, Liuzhou, 545001, People's Republic of China; [2]Department of Pharmacy, Shantou University Medical College, Shantou, 515041, People's Republic of China; [3]Department of Rehabilitation, Liuzhou Worker's Hospital, Liuzhou, 545001, People's Republic of China; [4]Department of Biotechnology and Food Engineering, Guangdong Technology Israel Institute of Technology, Shantou, 515063, People's Republic of China

*These authors contributed equally to this work

Correspondence: Jintao Zheng, Department of Biotechnology and Food Engineering, Guangdong Technology Israel Institute of Technology, Shantou, 515063, People's Republic of China, Tel +86 156 2584 9047, Email jintao.zheng@gtiit.edu.cn

Background: Radiotherapy is a widely used clinical tool for tumor treatment but can cause systemic toxicity if excessive radiation is administered. Although numerous nanoparticles have been developed as radiosensitizers to reduce the required dose of X-ray irradiation, they often have limitations, such as passive reliance on radiation-induced apoptosis in tumors, and little consider the unique tumor microenvironment that contributes radiotherapy resistance.

Methods: In this study, we developed and characterized a novel self-assembled nanoparticle containing dysprosium ion and manganese ion (Dy/Mn-P). We systematically investigated the potential of Dy/Mn-P nanoparticles (NPs) as a reactive oxygen species (ROS) amplifier and radiosensitizer to enhance radiation therapy and modulate the tumor microenvironment at the cellular level. Additionally, we evaluated the effect of Dy/Mn-P on the stimulator of interferon genes (STING), an innate immune signaling pathway.

Results: Physicochemical analysis demonstrated the prepared Dy/Mn-P NPs exhibited excellent dispersibility and stability, and degraded rapidly at lower pH values. Furthermore, Dy/Mn-P was internalized by cells and exhibited selective toxicity towards tumor cells compared to normal cells. Our findings also revealed that Dy/Mn-P NPs improved the tumor microenvironment and significantly increased ROS generation under ionizing radiation, resulting in a ~70% increase in ROS levels compared to radiation therapy alone. This enhanced ROS generation inhibited ~92% of cell clone formation and greatly contributed to cytoplasmic DNA exposure. Subsequently, the activation of the STING pathway was observed, leading to the secretion of pro-inflammatory immune factors and maturation of dendritic cells (DCs).

Conclusion: Our study demonstrates that Dy/Mn-P NPs can potentiate tumor radiotherapy by improving the tumor microenvironment and increasing endogenous ROS levels within the tumor. Furthermore, Dy/Mn-P can amplify the activation of the STING pathway during radiotherapy, thereby triggering an anti-tumor immune response. This novel approach has the potential to expand the application of radiotherapy in tumor treatment.

Keywords: radiotherapy, Dy/Mn-P NPs, ROS, tumor microenvironment, STING pathway

Introduction

Radiotherapy (RT) is a widely used method for treating cancer in contemporary clinical practice. Regrettably, despite its unparalleled curative efficacy, the therapeutic potential of this method is hindered by unfavorable adverse effects, most notably the health hazards associated with excessive radiation doses.[1,2] Recently, the use of NPs based on metal atoms with high atomic numbers in combination with radiation therapy to enhance the effect of radiation by accumulating or

Received: 5 October 2023
Accepted: 10 January 2024
Published: 22 January 2024

releasing more in the tumor site compared to healthy tissues can effectively increase the efficiency of radiotherapy and reduce side effects.[3–5] For instance, hafnium (Hf), gold (Au), and lanthanide elements have been developed as novel radio-sensitizing nanoparticles to effectively capture more local radiation dose inside the tumor since they possess a high atomic number, thus reducing the side effects of radiation therapy.[6–12] During the RT, these radiosensitizers can interact with X-ray via several physical processes, releasing electrons and generating ROS, leading to irreparable DNA lesions and inducing tumor cell apoptosis.[13–16] However, the unique tumor microenvironment (TME) poses challenges to the effectiveness of radiation therapy. For instance, the high levels of glutathione (GSH) and hydrogen peroxide (H_2O_2) within the tumor create an environment that hampers the efficacy of radiotherapy and promotes resistance to treatment.[17–20] Additionally, a lack of tumor sensitivity may result in increased toxicity to normal cells and tissues. Therefore, it is crucial for researchers to address these issues by developing radiotherapy sensitizers that exhibit selective toxicity towards tumor cells and regulate the TME.

As a local treatment for tumors, RT may be ineffective in addressing metastasized tumors owing to a lack of adequate immune response in clinical practice.[21–24] Fortunately, emerging evidence suggests that RT could activate the stimulator of STING pathway that acts as an innate immune signaling to induce the antitumor immune response against tumor cells when damaged tumor DNA escapes from the nucleus to the cytosol.[25–28] This discovery has opened up new possibilities for the clinical use of RT. However, in order to achieve adequate activation of the STING pathway, higher doses of X-ray radiation are usually required to increase the exposure of cytoplasmic DNA, which inevitably leads to irreversible damage to normal tissues and cells. It is reported manganese ion (Mn^{2+}) can directly activate cyclic GMP-AMP synthase (cGAS) and sensitize cGAS to recognize cytosolic DNA, achieving the activation of intracellular STING pathway.[29–32] In addition, recent studies further indicate that Mn^{2+} can efficiently kill cancer cells by converting endogenous H_2O_2 to highly toxic hydroxyl radicals (•OH) via a Fenton-like reaction. This property enables NPs based on Mn^{2+} ion to selectively kill tumor cells, as the concentration of H_2O_2 in normal cells is significantly lower than in tumor cells. During this progress, high valence ions manganese ion (Mn^{4+}) could be generated and then react with tumor endogenous GSH to re-convert as Mn^{2+}, leading to the generation of a substantial amount of ROS in tumor cells. This amplifies the ROS-induced damage to tumor cells and also plays a role in regulating TME-induced radiotherapy resistance.[33–35] Moreover, recent studies have revealed that inducing the formation of •OH during ionizing irradiation could enhance the overall radiotherapeutic effect.[9,10] From this point, the utilization of radiosensitizers in conjunction with Mn^{2+} shows great potential in developing tumor-targeted injury NPs that can activate the STING pathway and regulate the TME, ultimately leading to improved outcomes in radiation therapy.

Herein, sodium tripolyphosphate (STPP) was selected as phosphate ligands to coordinate with dysprosium ion (Dy^{3+}) as high atomic numbers and Mn^{2+} for the self-assembly of Dy/Mn-P in the presence of polyvinyl pyrrolidone (PVP) (Scheme 1). Firstly, the Dy/Mn-P could be rapidly degraded in the presence of acidic TME. Subsequently, the release of Dy^{3+}, a lanthanide element with a high atomic number (Z = 67), processes strong X-ray attenuation ability and better radio-sensitization effects for cancer cells to induce ROS generation and DNA damage. Secondly, the released Mn^{2+} could further convert tumor endogenous H_2O_2 into •OH, resulting in further damage to tumor cells and the formation of DNA lesions. Furthermore, Mn^{2+} could be oxidized high-valence Mn^{4+}. Subsequently, the reduction of Mn^{4+} to Mn^{2+} by intracellular GSH and buildup of oxidized glutathione (GSSG) initiate a secondary cascade of Fenton-like reactions and GSH depletion, thereby amplifying ROS damage for tumor cells and improving TME, ultimately enhancing radiotherapy. Thirdly, large amounts of cytoplasmic DNA are exposed, which synergize with Mn^{2+} to promote cytoplasmic DNA recognized by cGAS, triggering the activation of the STING pathway in cancer cells. Consequently, the expression of interferon type 1 (IFN-β) was upregulated to evoke an immune response. Our design strategy aims to extend the therapeutic boundaries of radiation therapy within the clinical setting, distinguishing it from previous studies that primarily focused on combined radiation therapy and immunotherapy.[36–38] In summary, our findings highlight the potential of our pH-responsive Dy/Mn-P to function as ROS amplifiers, effectively modulating the tumor microenvironment and augmenting the efficacy of tumor radiotherapy.

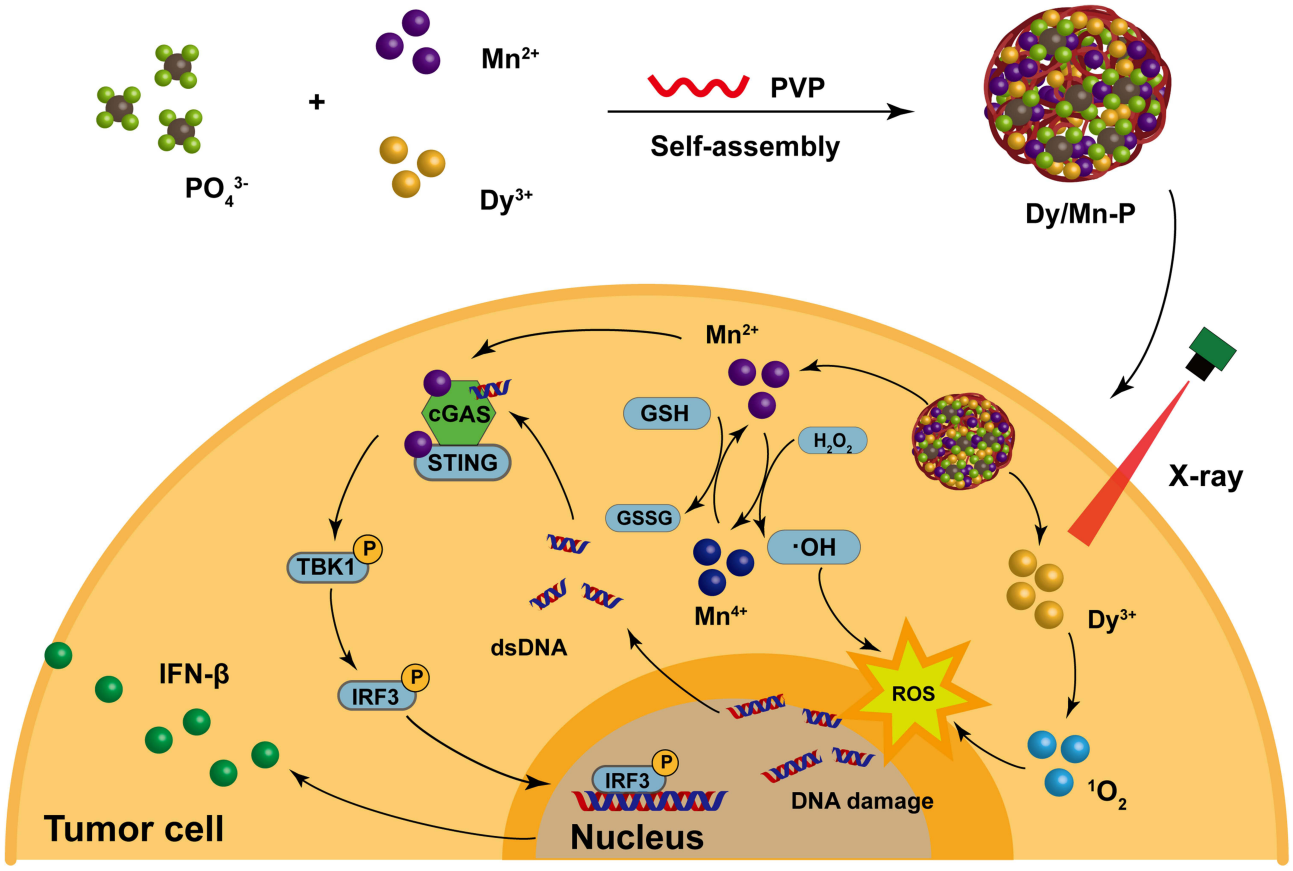

Scheme 1 The preparation of Dy/Mn-P (top) and the schematic illustration of the mechanism of Dy/Mn-P-mediated ROS amplifying, tumor microenvironment regulation, and cGAS-STING pathway activation (bottom).

Materials and Methods

Materials

Manganese chloride tetrahydrate ($MnCl_2{\cdot}4H_2O$) and Dysprosium chloride hexahydrate ($DyCl_3{\cdot}6H_2O$) were obtained from Aladdin (China). PVP and STPP were obtained by Macklin (China). Methylene blue (MB) was purchased from Acmec (China). Singlet oxygen sensor green (SOSG) was obtained from Invitrogen (USA). 4′,6-diamidino-2-phenylindole (DAPI) and Reactive oxygen species assay kit (catalog number CA1410) were purchased from Solarbio (China). Calcein AM and propidium iodide (PI) cell viability/cytotoxicity assay kit (catalog number C2015S), fluorescein isothiocyanate Annexin V-FITC/PI kit, and DNA damage assay kit by γ-H2AX Immunofluorescence were supplied by Beyotime (China). Fetal bovine serum (FBS) was purchased from Newzerum (New Zealand). Cell counting kit-8 (CCK-8) was purchased from DojinDO (Japan). Micro BCA protein assay kit was obtained by Thermo Fisher Scientific (USA), and Prestained protein ladder was purchased from Yeasen Biotechnology (catalog number: 20350ES72). Rabbit anti-phospho-TBK1 (Ser172) antibody (catalog number bs-3440R), Rabbit anti-phospho-IRF3 (Ser396) antibody (catalog number bs-3195R), Rabbit anti-TBK1 antibody (catalog number bs-7497R), and Rabbit anti-IRF3 antibody (catalog number bs-2993R) were purchased from Bioss (China). Rabbit anti-IFN-β antibody (catalog number) was purchased from Abcam (USA). Mouse IL-6 and TNF-α ELISA kit were purchased from Elabscience (China).

Self-Assembly of Dy/Mn-P NPs

10 μL of $MnCl_2{\cdot}4H_2O$ (0.5 M) and $DyCl_3{\cdot}6H_2O$ (0.5 M), 125 μL of PVP (2 mM), and 20 μL of STPP (1 M) were prepared as 500 μL mixture solution. The mixture was stirred at 900 rpm for 60 min at 37 °C. Then, Dy/Mn-P NPs were obtained by centrifuging at 5000 rpm for 10 min, washed 3 times in ultrapure water, and dried at 40 °C. Moreover, NPs were optimized by using different ratios of Mn^{2+} and Dy^{3+} to get suitable particle size and dispersion.

Characterization of Dy/Mn -P NPs

Transmission electron microscopy (TEM, JEM-F200, Japan) and scanning electron microscopy (SEM, SU-70, Japan) were used to observe the surface morphology and size of Dy/Mn-P, while chemical composition was analyzed by energy-dispersive spectrometer (EDS). The average hydrodynamic diameter and zeta potential of Dy/Mn-P were measured by the Malvern Zetasizer Ultra instrument (Malvern, UK).

Stability and ROS Detection

About 70 μg/mL of Dy/Mn-P was dispersed in 2 mL acetate buffer solution with different pH values (4.8 and 7.5) containing 10% FBS at room temperature. The change in particle size and dispersion was measured every 12 h until 72h. As for ROS detection, 12.5 mM $NaHCO_3$, 25 μg/mL MB, 0–20 μg/mL Dy/Mn-P, and 0–10 mM H_2O_2 solution were prepared as 1 mL solution, and then the mixture was incubated with stirring at 200 rpm and 37 °C in the dark for different time. The change in absorbance value at 664 nm was detected at the appointed time to evaluate the generation of •OH. To observe the generation of singlet oxygen ($^1O_2$), 10 μL SOSG (500 μM) was added to 990 μL Dy/Mn-P NPs (5 μg/mL). After exposure to different X-ray irradiation (0–6 Gy), the fluorescence intensity was detected in SPARK Microplate Reader (TECAN, Switzerland).

Cell Lines

Breast cancer cells (4T1), fibroblast cells (3T3) and melanoma cells (B16-F10) were obtained from the American Type Culture Collection (ATCC, Manassas, USA). DC2.4 cells were purchased from Kanglang Biological Technology Co., Ltd. (Shanghai, China). 4T1, B16-F10, and DC2.4 cells were cultured in RPMI 1640 medium containing 10% FBS and 3T3 cells were cultured in DMEM medium containing 10% FBS. All cells were cultured at 37 °C and 5% CO_2 in a humidified atmosphere.

Cytotoxicity and Cellular Uptake

B16-F10, 4T1, 3T3, and DC2.4 cells were seeded into 96-well plates at a density of 1×10^4 per well. After 24 h cultured, the culture medium was replaced with fresh cell culture medium containing different concentrations of Dy/Mn-P (0–500 μg/mL) and co-cultured for 24 h. Then, the cells were washed twice with PBS and cultured with CCK-8 working fluid for a suitable time. The absorbance value at 450 nm was determined by SPARK Microplate Reader. The cell viability was calculated based on the following formula:

$$Cell\ viability = \left(OD_{450nm\ of\ the\ sample} - OD_{450nm\ of\ blank}\right) / \left(OD_{450nm\ of\ control} - OD_{450nm\ of\ blank}\right) \times 100\%.$$

Meanwhile, B16-F10 cells were treated with Calcein-AM and PI after treatment with Dy/Mn-P NPs at a concentration of 70 μg/mL to further observe the ratio of live or dead cells by using fluorescence microscopy (Axio observer A1, ZEISS, Germany). As for analysis of apoptosis, Annexin V-FITC/PI kit was used to stain the cells, and the frequency of cell apoptosis was detected by flow cytometry (Accuric6, BD).

To evaluate the cellular uptake of Dy/Mn-P NPs, the B16-F10 cells were seeded in a cell culture dish at a density of 5×10^4 and cultured for 12 h. Following this, the medium was replaced with 1mL of RPMI-1640 medium containing 70 μg/mL Dy/Mn-P tagged with Rhodamine B dye (RhB) for different times (0, 2, 4 h). Then, the medium was removed and the cells were washed three times with 1× PBS (4 °C) and fixed with 1 mL of 4% paraformaldehyde solution (purchased from Solarbio, China) for 10 min. Next, 1 mL of DAPI working solution (1 μg/mL) was added to the cells and cultured for 5 min. Finally, the cells were washed three times with 1× PBS (4 °C) and observed by a confocal laser scanning microscope (LSM880, ZEISS, Germany). Additionally, the fluorescence value change of B16-F10 cells was analyzed by cell flow cytometry after treatment with Dy/Mn-P NPs for varying periods.

Clonogenic Assay

For the clonogenic assay, B16-F10 cells were seeded into 6-well plates at the densities of 500 per well and incubated at 37 °C for 24 h. Then, B16-F10 cells were treated with 70 μg/mL of Dy/Mn-P NPs for 4 h, while cells treated with 1× PBS were as the control. Next, the cells were exposed to X-ray irradiation with radiation doses of 6 Gy. After further incubation for 7 days at 37 °C, the cells were fixed with 4% paraformaldehyde and stained with crystal violet (Solarbio,

China). The results of cell colonies were calculated only if they contained more than 50 cells. The surviving fraction was calculated as follows:

$$Survival\ rates = (surviving\ colonies)/(cells\ seeded \times\ plating\ efficiency) \times 100\%$$

The mean surviving fraction was obtained from three parallel tests.

Cellular ROS and GSH

B16-F10 cells (5×10^4 per dish) were plated in 24-well plates and treated with 70 μg/mL of Dy/Mn-P for 4 h. Untreated cells were regarded as control. Afterward, the cells were treated with a 6 Gy dose of X-rays and incubated for another 8 h. According to the manufacturer's protocol, B16-F10 cells were washed three times with PBS and incubated with PBS containing 10 μM 2′,7′-dichlorodihydrofluorescein diacetate (H2DCFDA) for 30 min in the dark. ROS level was evaluated by fluorescence microscopy. Additionally, the ROS fluorescence value of B16-F10 cells was analyzed by cell flow cytometry. The GSH of B16-F10 cells was observed by fluorescence microscopy by using ThiolTrace Violet as a detection reagent after treatment with Dy/Mn-P NPs as above. The tumor oxidative damage caused by Dy/Mn-P NPs was further evaluated by JC-1 dye after exposure to X-ray (6 Gy) and observed by fluorescence microscopy.

γ-H2AX Staining for DNA Fragments

B16-F10 cells (5×10^4 per dish) were incubated in 24-well plates after incubating with 70 μg/mL of Dy/Mn-P NPs for 6 h. Then, the cells were exposed to X-ray irradiation at the dose of 6 Gy and cultured for another 18 h. The treated B16-F10 cells were fixed by 4% paraformaldehyde and then labeled with the anti-phospho-histone γ-H2AX mouse monoclonal antibody as the primary antibody overnight at 4 °C. After washing with 1× PBS (4 °C), the B16-F10 cells were further incubated with sheep anti-mouse secondary antibody for 1 h at 37 °C. Meanwhile, cell nuclei were stained by DAPI for imaging via using fluorescence microscopy.

cGAS-STING Pathway Activation

In a direct co-culture system, B16-F10 cells (3×10^5 per dish) were co-cultured with DC2.4 cells (1×10^4 per dish) in 6-well plates for 48 h followed by treatment with 1× PBS and Dy/Mn-P NPs (70 μg/mL) for 4 h. Then, co-cultured cells were further cultured for another 8 h after irradiated with a dose of 6 Gy. Protein samples were harvested by adding 100 μL RIPA lysis buffer containing 1 × PMSF and 1 × PSIM and ultrasonic crushing. The same concentration of protein samples was separated by SDS polyacrylamide gel electrophoresis after being quantified by a Micro BCA protein assay kit and blotted onto polyvinylidene fluoride membrane (Millipore). The membrane was blocked with 5% non-fat milk in tris-buffered saline with 0.1% Tween 20 (TBST) at room temperature for 1 h and then treated with corresponding antibodies at 4 °C overnight, including Actin polyclonal antibody (1:1000), phospho-IRF3 (ser396) polyclonal antibody (1:1000), phosphor-TBK1 (ser172) polyclonal antibody (1:1000), IRF3 polyclonal antibody (1:1000), TBK1/NAK polyclonal antibody (1:1000) and IFN-β monoclonal antibody (1:1000). After that, it was washed three times with 1×TBST, and then treated with the corresponding secondary antibody. Finally, the protein bands were visualized with ECL reagent (Thermo Fisher Scientific, USA) by the Chemidoc XRS gel imaging system (Bio-rad, USA). The relative protein expression level was quantified by using Image J software. Meanwhile, the supernatant was collected after treatment with X-ray irradiation and the cytokine including TNF-a and IL-6 were measured by the corresponding ELISA kit. For dendritic cells maturation evaluation, DC2.4 cells were cultured in 24-well plates, and the supernatant of different treated co-culture cells was added to DC2.4 cells for 24 h. Then, the cells were collected and stained with anti-mouse CD11c FITC (11–0114-82, Invitrogen), anti-mouse CD80 APC (17–0801-81, Invitrogen), and anti-mouse CD86 PE (12–0862-83, Invitrogen) antibodies. Finally, the frequency of matured DCs was evaluated by flow cytometry.

Statistical Analysis

All quantitative results are expressed as the mean ± standard deviation (SD). The statistical analysis was performed by one-way ANOVA using GraphPad Prism (8.0), and the statistical significance was defined as $*P < 0.05$; $**P < 0.01$; $***P < 0.001$.

Results and Discussion

Synthesis and Characteristics of Dy/Mn-P NPs

Initially, NPs with different molar mass ratios of Dy^{3+} to Mn^{2+} (5:1–1:5) were prepared to investigate the dispersion and size. As shown in Figure S1, a series of different size of Dy/Mn-P NPs ranging from ~180 to ~1200 nm were successfully synthesized, which may result from different size between Dy and Mn ions themselves.[39] Among those NPs, the obtained Dy/Mn-P NPs at a ratio of Dy^{3+} to Mn^{2+} (1:1) exhibited well dispersity and uniform spherical morphology where hydrodynamic diameter of Dy/Mn-P was 180 ± 0.64 nm with a polymer dispersity index (PDI) less than 0.3 and the zeta potential was −28.25 ± 0.54 mV, according to dynamic light scattering (DLS) analysis (Figures 1A and B). Subsequently, the surface morphology of Dy/Mn-P NPs was observed through TEM and SEM. It revealed that the synthesized Dy/Mn-P were homogeneous in shape with a particle size of ~70 nm (Figures 1C and S2). After that, the chemical composition of Dy/Mn-P was also a major concern to reflect their physicochemical properties. Form the elemental mapping images in Figure 1D, the homogenous and well-overlapped distribution of Dy, Mn, P, and O elements in Dy/Mn-P demonstrated the successful fabrication of Dy/Mn-P with Mn and Dy ions doped nanostructure. EDS spectrum further confirmed the presence of Mn and Dy elements in the prepared Dy/Mn-P (Figure S3). X-ray diffraction (XRD) pattern in Figure S4 revealed that Dy/Mn-P presented broad hump from 15° to 40° without obvious diffraction peaks, indicating their amorphous nature. In addition, as shown in Fourier transform infrared (FTIR) spectroscopy (Figure S5), some characteristic peaks were displayed in STPP including a peak at around 1170 cm^{-1} belonging to P=O stretching vibration, a peak near 897 cm^{-1} that indicated at P-O stretching vibration, and six medium-intensity peaks between 400 and 740cm.$^{-1}$[40,41] In the spectra of Dy/Mn-P, the characteristic peaks at 1670, 1421, and 1290 cm^{-1} belonging to the stretching vibration of C=O, C-H, and C-N in traditional PVP framework, respectively.[42] Meanwhile, the absorption peak at 556 cm^{-1} in Dy/Mn-P was assigned to the stretching vibration of Mn-O and Dy-O, further demonstrating the successful preparation of Dy/Mn-P.[43,44]

The pH-sensitive responsive of NPs under acidic conditions is beneficial in reducing the damage to normal tissues due to the tumor microenvironment which usually exhibits acidity. As shown in Figures 1E and S6, no significant particle size and PDI change were seen in Dy/Mn-P after incubating with acetate buffer solution with 10% FBS at pH = 7.5 for 72 h. Comparably, when Dy/Mn-P was exposed to acetate buffer solution (pH = 5.0), the size of Dy/Mn-P gradually increased and PDI also increased to 0.65, which indicated that Dy/Mn-P possess pH-sensitivity and easily disintegrated under acidic conditions. This may be related to the weakening of the bonding between phosphorus and metal ions at low pH values.

ROS Trigged by Dy/Mn-P NPs

During RT, the released electrons react with organic molecules or water in cancer cells to produce ROS, especially $^1O_2$, which could be evaluated by using the SOSG probe, a highly selective detection reagent for $^1O_2$.[45,46] As shown in Figures 1F and S7, the fluorescence intensity change of SOSG revealed generation of $^1O_2$ after exposing to radiation doses from 0 to 6 Gy in the presence of Dy/Mn-P at concentration of 5 μg/mL. Notably, it was found that the maximum generation of ROS capacity via Dy/Mn-P increased 14-fold after X-ray irradiation at radiation dose of 6 Gy compared to the control group. Therefore, 6 Gy was selected as appropriate radiation doses in subsequent experiments. Moreover, the generation of $^1O_2$ in the presence of Dy/Mn-P NPs under 6 Gy X-ray irradiation was further verified by electron spin resonance (ESR) spectroscopy in Figure 1G. A typical 1:1:1 peak signal representing $^1O_2$ was observed by using triacetonamine hydrochloride as a trapping agent which was attributed to the high Z lanthanide element in the Dy/Mn-P absorbing more X-ray irradiation and subsequently releasing more electrons such as photoelectrons and oxygen electrons to react with organic molecules. In addition, tumor endogenous high expression of H_2O_2 can be converted into •OH through a Fenton-like reaction induced by Mn^{2+}, which facilitates the reduction of radioresistance.[47–49] To explore the conversion of H_2O_2 into •OH caused by Dy/Mn-P, MB was selected as an indicator to evaluate the generation of •OH that lead to the decrease in the absorbance of MB at 664 nm. As shown in Figure S8 the progressively increased degradation of MB could be observed by co-incubating H_2O_2 and Dy/Mn-P at room temperature with 120 min, implying that Dy/Mn-P can catalyze H_2O_2 to generate •OH due to the presence of Mn^{2+}. Moreover, the absorbance spectra of MB exhibited

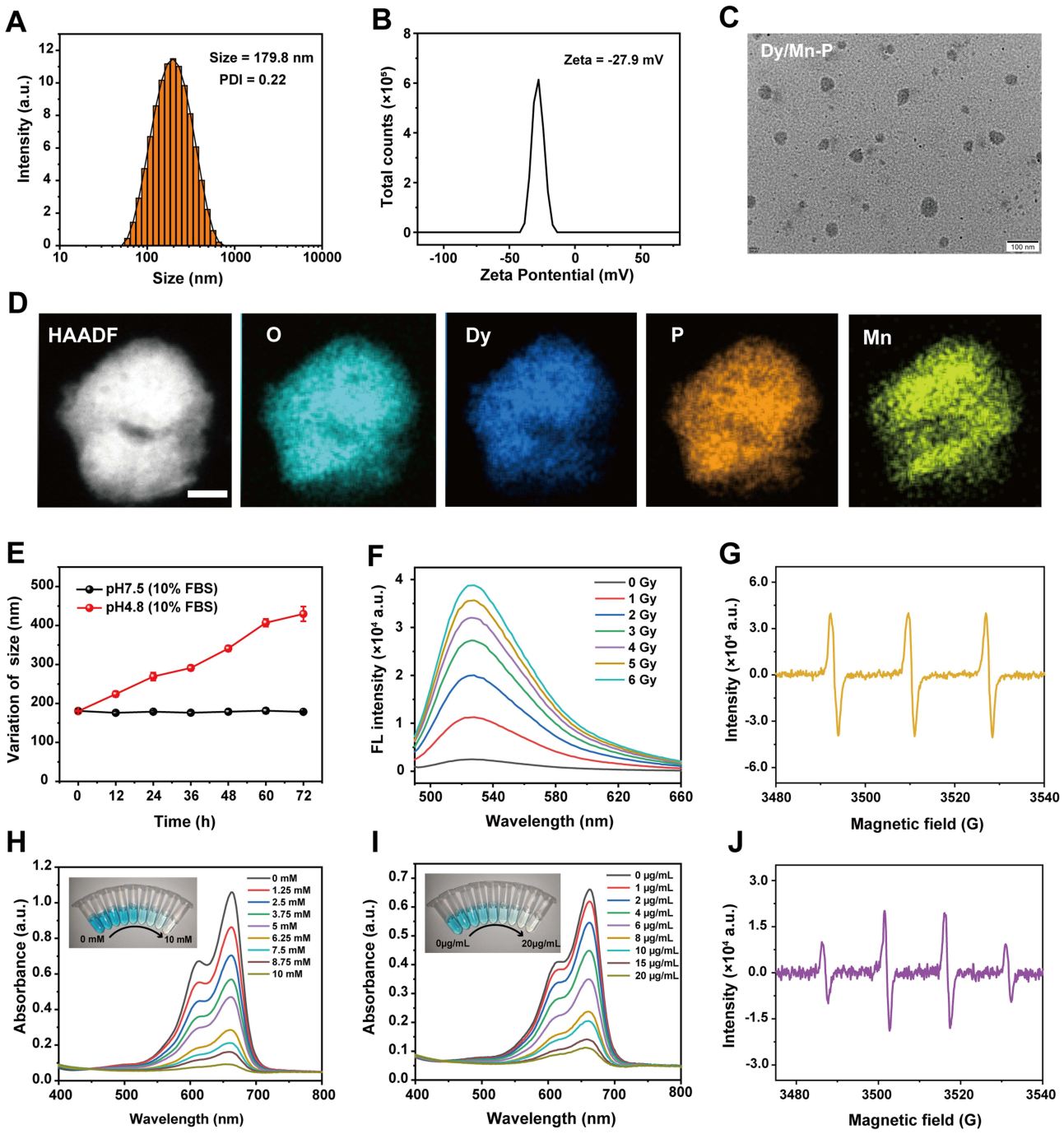

Figure 1 Synthesis and characterization of Dy/Mn-P. (**A** and **B**) Representative graphs of size distribution and zeta potentials of Dy/Mn-P, respectively. (**C**) TEM image of Dy/Mn-P. Scale bar = 100 nm. (**D**) HAADF-STEM image and elemental mapping for Dy/Mn-P. Scale bar = 20 nm. (**E**) Hydrodynamic size values of Dy/Mn-P in acetate buffer solution with 10%FBS at different pH values (7.5 and 4.8) for 72 h. (**F**) The generation of $^1O_2$ caused by Dy/Mn-P after exposing to different radiation doses. (**G**) ESR spectrum of Dy/Mn-P exposed to 6 Gy X-ray radiation to observe $^1O_2$ peaks. (**H** and **I**) Absorbance spectra change of MB under different concentrations of H_2O_2 or different concentrations of Dy/Mn-P. (**J**) ESR spectrum of Dy/Mn-P exposed to 6 Gy X-ray irradiation to observe •OH peaks.

gradient changes after exposing various concentrations of H_2O_2 and Dy/Mn-P (Figures 1H and I). A 1:2:2:1 quadruplet signal, identified as DMPO-OH, was observed by ESR in Figure 1J after using 5,5-dimethyl-1-pyrroline-N-oxide (DMPO) as a trapping agent, further revealing the generation of •OH. This was conducive to tumor-selective treatment due to the high-level concentration of tumor endogenous H_2O_2 compared to normal tissue.

https://doi.org/10.2147/IJN.S436160 DovePress

Cytotoxicity and Cellular Uptake of Dy/Mn-P NPs

B16-F10, 4T1, 3T3, and DC2.4 cells were treated with different concentrations of Dy/Mn-P from 0 to 500 μg/mL for 24 h to evaluate cytotoxicity by CCK-8 assay. Encouragingly, positive cytotoxicity was observed in tumor cells, including B16-F10 cells with a median inhibitory concentration (IC_{50}) of ~68.28 μg/mL (Figures 2A and S9A) and 4T1 cells with an IC_{50} of ~83.45 μg/mL (Figures 2B and S9B). However, for normal cells, both 3T3 and DC2.4 cells exhibited lower toxicity compared to tumor cells where the IC_{50} was 196.2 μg/mL for 3T3 cells (Figures 2C and S9C) and 146.7 μg/mL for DC2.4 cells, respectively (Figures 2D and S9D). It indicated that Dy/Mn-P has selectivity treatment for cancer cells, which may be attributed to the higher level of endogenous H_2O_2 in tumor cells compared to normal cells and the degradation of Dy/Mn-P due to the acidic tumor microenvironment. B16-F10 cells were used to further investigate the cellular internalization behavior of Dy/Mn-P labelled with RhB by using CLSM and flow cytometry. According to the image of CLSM, the RhB fluorescence signal (red) gradually increased within 4 h in B16-F10 cells, which demonstrated time-dependent cellular internalization of Dy/Mn-P (Figure 2E). In addition, the quantification of the fluorescence intensity of B16-F10 cells was evaluated by flow cytometry at 0, 2, and 4 h. it revealed that the cellular uptake of Dy/Mn-P at 4 h was 1.4 times higher than that at 2 h (Figures 2F and G). These results suggest the efficient delivery and tumor-selective cytotoxicity of Dy/Mn-P.

Radiosensitization Effect of Dy/Mn-P NPs

The calcein-AM and PI probe was performed to assess Dy/Mn-P-mediated radiosensitization inducing apoptosis in B16-F10 cells. In this assay, live cells can be stained by calcein AM and imaged with green fluorescence, while necrotic cells were stained with PI to observe red fluorescence. The control (+) group (X-ray irradiation alone) and Dy/Mn-P (-) group could cause B16-F10 cells apoptosis and necrosis compared to the control group, while the highest red fluorescence was observed in the Dy/Mn-P combined with X-ray irradiation (Figure 3A). Furthermore, apoptosis and necrosis cells were evaluated by the apoptosis detection kit. Early apoptotic cells were only stained with Annexin V-FITC, while late apoptotic and necrotic cells were stained with Annexin V-FITC and PI as analyzed by flow cytometry. As shown in Figures 3B and C, the apoptosis and necrosis rate were increased from the original 0.26% to 7.54% after only treatment with Dy/Mn-P for 24 h. However, a significant apoptosis and necrosis rate (13.9%) was elicited in Dy/Mn-P plus X-ray irradiation. Our results indicate that the Dy/Mn-P NPs can greatly induce tumor cell apoptosis and necrosis under X-ray irradiation. In addition, the ability of tumor cells to proliferate rapidly and divide "indefinitely" is one of the reasons for tumor treatment failure.[50] The cell clone formation in Figure 3D reveals that compared to the control group, only 20% of the cell survival fraction was reduced when accepted X-ray irradiation alone. However, the cell survival fraction in the Dy/Mn-P (-) group was reduced to about 23%, attributed to the Mn ion-mediated Fenton-like reaction. It is noteworthy that only a few viable colonies were formed in the Dy/Mn-P (+) group with the tumor cell survival fraction was less than 8% (Figures 3D and E), which further indicated that Dy/Mn-P effectively sensitized to radiotherapy to induce cancer cell death and inhibit tumor cell rapid proliferation owing to generate effective products in the presence of X-ray irradiation.

Endogenous ROS Generation and GSH Depletion

The cellular ROS generation and GSH depletion induced by Dy/Mn-P were investigated by corresponding probes. H2DCFDA is a sensitive fluorescent probe for the detection of intracellular ROS levels. A slight green fluorescence was detected in the control (-) group or control (+) group, suggesting X-ray irradiation alone made it difficult to produce satisfactory ROS levels to meet clinical needs. However, a stronger green fluorescence signal was observed in B16-F10 cells after incubating with Dy/Mn-P which was main attributed to the Mn^{2+}-induced Fenton-like reactions[51] The strongest fluorescence signal was observed in the Dy/Mn-P (+) group, demonstrating the highest ROS generation level after exposing to X-ray irradiation (Figure 4A). In addition, the result of flow cytometry was further used to prove the highest intensity of cellular endogenous ROS levels after treatment with Dy/Mn-P plus X-ray irradiation (Figures 4C and D). Therefore, the application of Fenton process significantly increases the ROS production and combination with lanthanides can maximize amplification of intracellular ROS levels under the X-ray irradiation due to release of secondary electrons.[10,11]

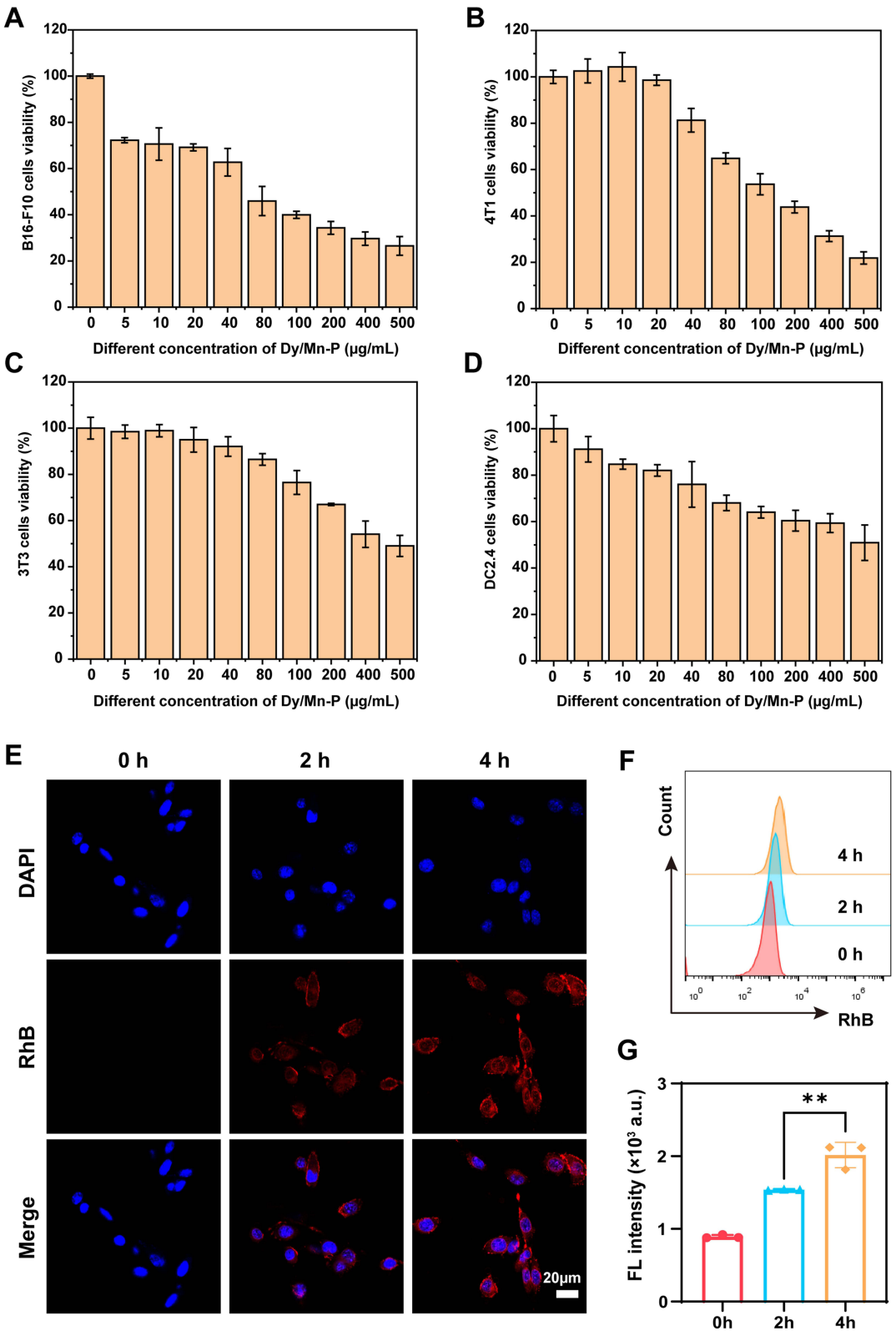

Figure 2 Cytotoxicity and cellular uptake of Dy/Mn-P. (**A-D**) The cytotoxicity of B16-F10 cells, 4T1 cells, 3T3 cells, and DC2.4 cells after treatment with different concentrations of Dy/Mn-P NPs (0–500 μg/mL). Data represent means ± SD (n = 3). (**E**) CLSM images of B16-F10 cells incubated with RhB-labelled Dy/Mn-P at different times. Scale bar = 20 μm. (**F** and **G**) Representative flow cytometry plots and quantitative fluorescence analysis of B16-F10 cells incubated with RhB-labelled Dy/Mn-P for different times (n = 3). Statistical significance was calculated via one-way ANOVA with Tukey's test: $^{**}P < 0.01$.

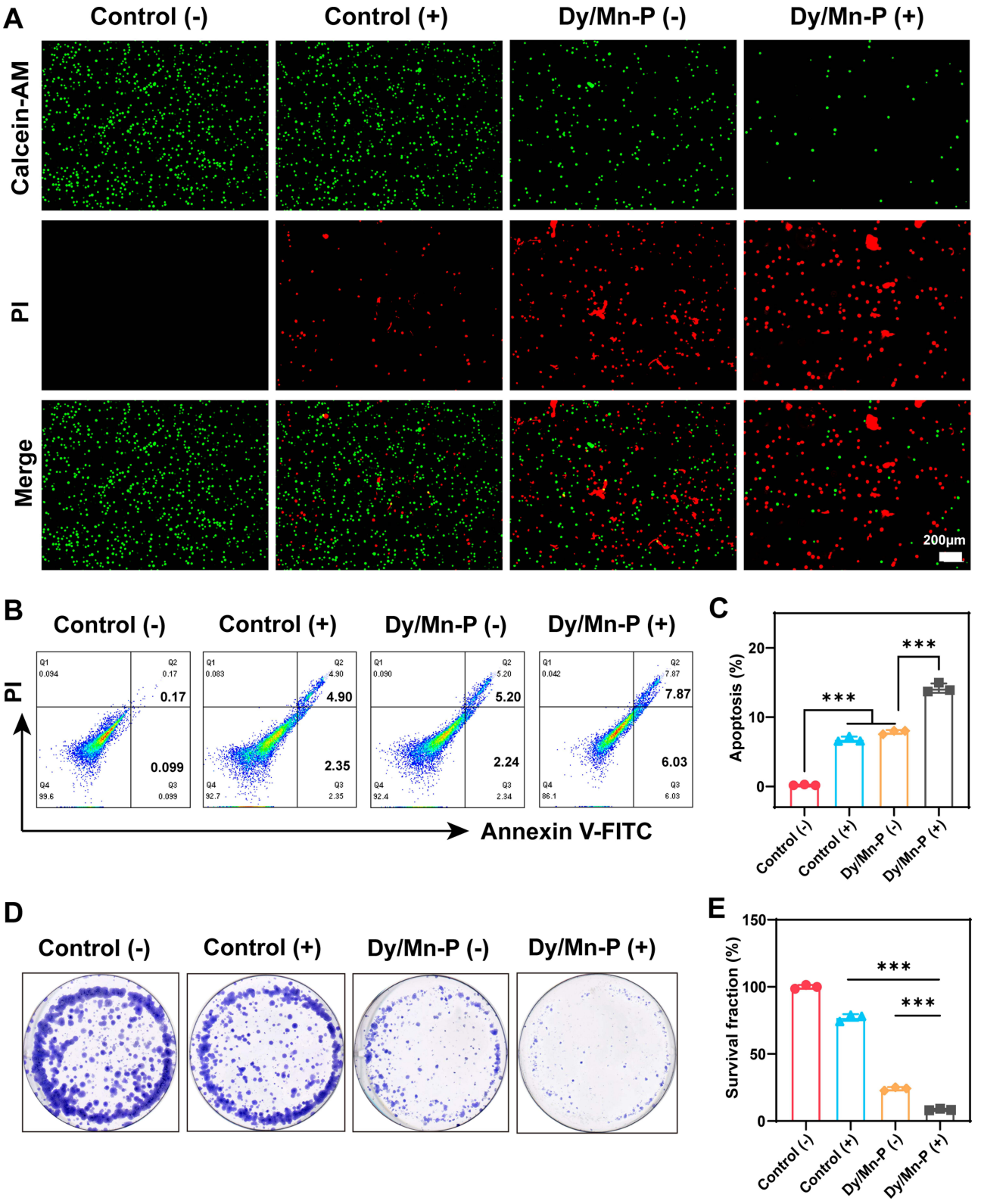

Figure 3 In vitro radiosensitization effect of Dy/Mn-P. (**A**) Live/dead cells assay after various treatments, in which (-)/(+) indicated without/with X-ray irradiation. Scale bar = 200 μm. (**B** and **C**) Representative flow cytometry plots and quantitative apoptosis analysis of B16-F10 cells by staining with Annexin V-FITC and PI after different treatments (n = 3). (**D** and **E**) Colony formation of B16-F10 cells after various treatments indicated and the corresponding survival fraction. Data were given as mean ± SD (n = 3). Statistical significance was calculated via one-way ANOVA with Tukey's test: ***P < 0.001.

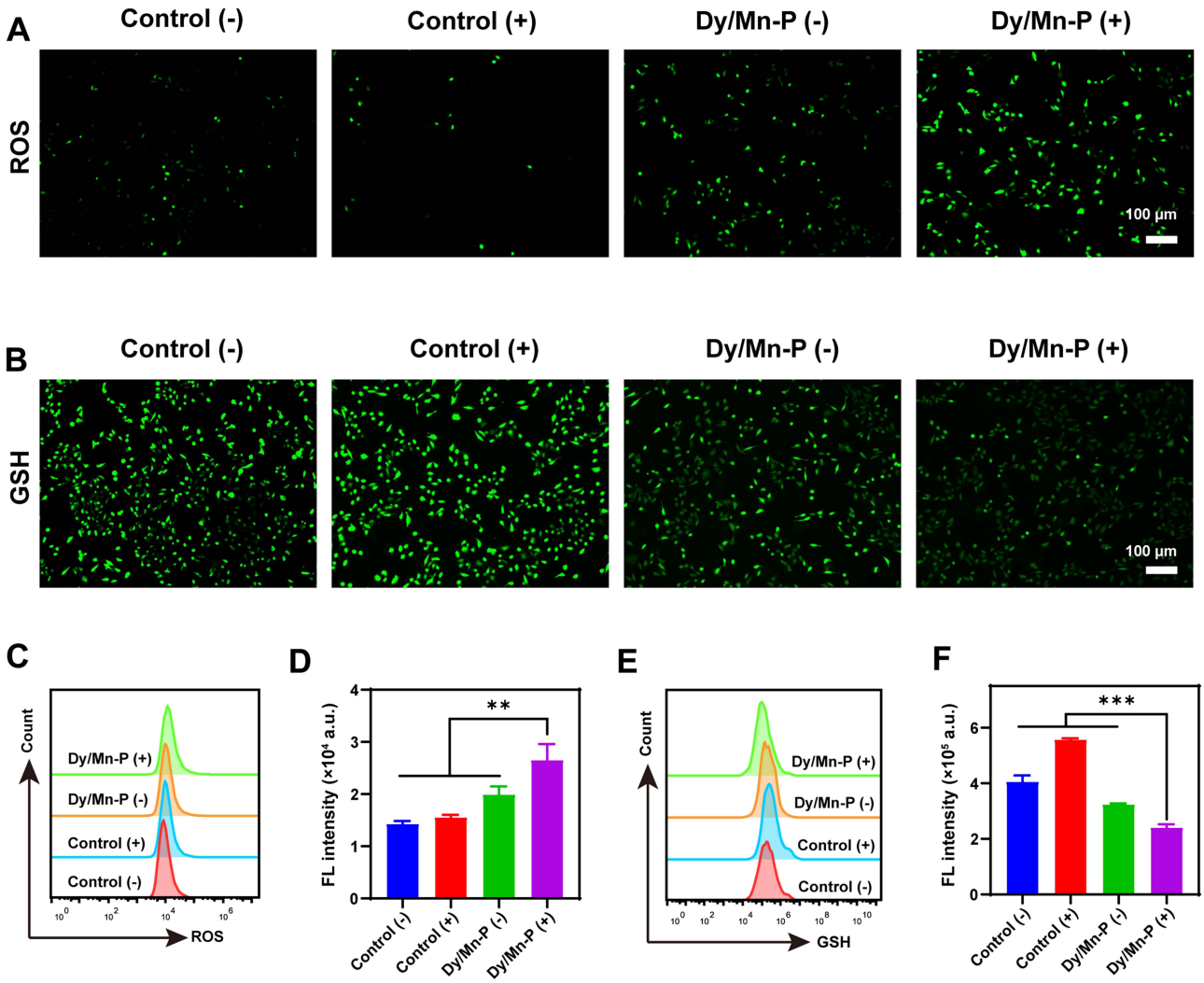

Figure 4 Endogenous ROS generation and GSH depletion caused by Dy/Mn-P. (**A**) Fluorescence images of intracellular ROS production. Scale bar = 100 μm. (**B**) Fluorescence images of intracellular GSH depletion. Scale bar = 100 μm. (**C** and **D**) Representative flow cytometry plots and quantitative fluorescence analysis of ROS generation in B16-F10 cells. Data were given as mean ± SD (n = 3). (**E** and **F**) Representative flow cytometry plots and quantitative fluorescence analysis of GSH depletion in B16-F10 cells. Data were given as mean ± SD (n = 3). Statistical significance was calculated via one-way ANOVA with Tukey's test: $^{**}P < 0.01$; $^{***}P < 0.001$.

Notably, evidence from recent studies has proved that tumor endogenous GSH is a prominent means of scavenging ROS, thereby reducing ROS damage to tumor cells.[52] Therefore, depletion of intracellular GSH makes cancer cells more susceptible to oxidative stress. To further confirm that GSH scavenging was triggered by the progress of the valence transition of Mn ions, the ThiolTrace Violet was selected as a sensitive and reproducible fluorescence probe to investigate GSH levels in B16-F10 cells after different treatments. As shown in Figure 4B, when exposed to X-ray irradiation alone, there was an obvious increase in intracellular GSH content compared to the control group, suggesting the fact that radiation therapy alone is highly susceptible to radio-resistance, leading to treatment failure. However, the depletion of GSH levels was observed in Dy/Mn-P (-) and Dy/Mn-P (+), which were caused by Mn ions in high valence states (Mn^{4+}). It indicated that the doping of Mn ions in Dy/Mn-P could effectively reduce endogenous GSH while increasing ROS levels thus enhancing oxidative damage in tumor cells, leading to DNA damage enhancement. The endogenous GSH levels were quantified by flow cytometry to further prove the highest depletion of GSH in Dy/Mn-P (Figures 4E and F). These results suggest that Dy/Mn-P NPs can act as a ROS amplifier to improve radiation resistance induced by the tumor microenvironment and enhance the tumor radiotherapy.

Mitochondrial Membrane Potential Changes and DNA Damage

Mitochondria are important mediators of cellular metabolism and generators and targets of ROS. In first, the JC-1 dye was used to assess mitochondrial membrane potential changes induced by Dy/Mn-P, where red fluoresce was shown in normal cellular mitochondria via J-aggregates, and green fluorescence of J-monomers indicated abnormal mitochondrial function. As shown in Figure 5A, a significant decrease in red fluorescence and an increase in green fluorescence were observed in the Dy/Mn-P (+) group compared to other groups, indicating that Dy/Mn-P enhanced mitochondrial damage after exposing to X-ray irradiation, which was associated with ROS amplification and accumulation effect triggered by Dy/Mn-P. Phosphorylated H2AX histone (ie, γ-H2AX) is a key marker of radiation-induced DNA double-strand breaks.[53] The formation of γ-H2AX foci was further detected by immunofluorescence (green fluorescence). No fluorescent signal was observed in the control (-) group, while a slight green fluorescence was detected in the control (+) group and Dy/Mn-P group owing to DNA damage induced by X-ray irradiation directly and ROS. Notably, high levels of γ-H2AX-positive foci in the nucleus were imaged after treatment with Dy/Mn-P plus X-ray irradiation, suggesting that Dy/Mn-P could enhance DNA damage in tumor cells and reduce the radiation resistance under X-ray irradiation (Figure 5B). All these results together proved that the combination of Dy/Mn-P and X-ray irradiation could induce robust tumor oxidative damage and promote DNA damage. Moreover, it has been reported that cytosolic DNA release could be recognized by cGAS to activate the STING pathway to induce DCs maturation and stimulation anti-tumor immune response.[54]

STING Activation and DCs Maturation

Subsequently, we explored the stimulation of the cGAS/STING pathway by Western blot after different treatments. The phosphorylated IRF-3 (p-IRF3) and phosphorylated TBK1 (p-TBK1) are two important downstream transcription factors in the STING pathway, responding to the degree of STING pathway activation and triggering the secretion of IFN-β, which could induce DCs maturation, improve pro-inflammatory cytokines secretion, such as TNF-α and IL-6, and generate a series of anti-tumor immunity.[55,56] To mimic the tumor environment, B16-F10 cells and DC2.4 cells were co-cultured to investigate the activation of the STING pathway in tumor cells. It was found that the expression of p-TBK1, p-IRF3, and IFN-β protein was slightly increased in co-cultured cells after only receiving Dy/Mn-P treatment, which was attributed to Mn^{2+} can directly activate the STING pathway.[30] Meanwhile, the expression of both p-TBK1 and p-IRF3 was significantly increased in the Dy/Mn-P (+) group. It indicated that massive exposure of cytoplasmic DNA induced by radio-sensitization of Dy ions, which were sensitized by Mn^{2+} and realized stimulation of the STING pathway (Figures 6A-F). The secretion of TNF-α and IL-6 in the co-cultured cells supernatant was evaluated by the corresponding ELISA Kit. As shown in Figures 6G and H, compared to other groups, the secretion level of TNF-α and IL-6 was significantly enhanced in the Dy/Mn-P (+) group. More importantly, a significant increase in the proportion of matured DCs was observed after incubating with co-cultured cells supernatant treated by Dy/Mn-P NPs plus X-ray irradiation (Figure 6I and J). Dy/Mn-P (-) group could directly induce 20.1% DCs maturation owing to stimulation of the STING pathway by Mn^{2+}. Of note, 28.7% DCs maturation was observed in the Dy/Mn-P (+) group, which is approximately 3.2 times that of the control group (9.06%). Although X-ray irradiation alone could induce slight immune response, it only increased the maturation of DCs by 6.5% compared to the control group, which is far from adequate for clinical needs. These results together evidenced that the combination of Dy/Mn-P and X-ray irradiation-induced STING pathway activation and striking secretion of IFN-β and then resulted immune response.

Conclusions

In this study, we develop Dy/Mn-P NPs as ROS amplifiers to regulate tumor microenvironment and enhance tumor radiotherapy by three different aspects: (1) Dy/Mn-P NPs can rapidly be degraded at acidic tumor environments resulting in lanthanide radiosensitizer (Dy^{3+}) and Mn^{2+} release. (2) Dy/Mn-P NPs exhibit a tumor-selective therapeutic capacity and significant radiotherapy sensitization effect on tumor cells. (3) Dy/Mn-P NPs can induce endogenous GSH depletion and ROS accumulation in tumors, thereby improving radiotherapy resistance triggered by tumor microenvironment. In addition, damaged tumor DNA escapes from the nucleus owing to RT and ROS, which further activate the STING

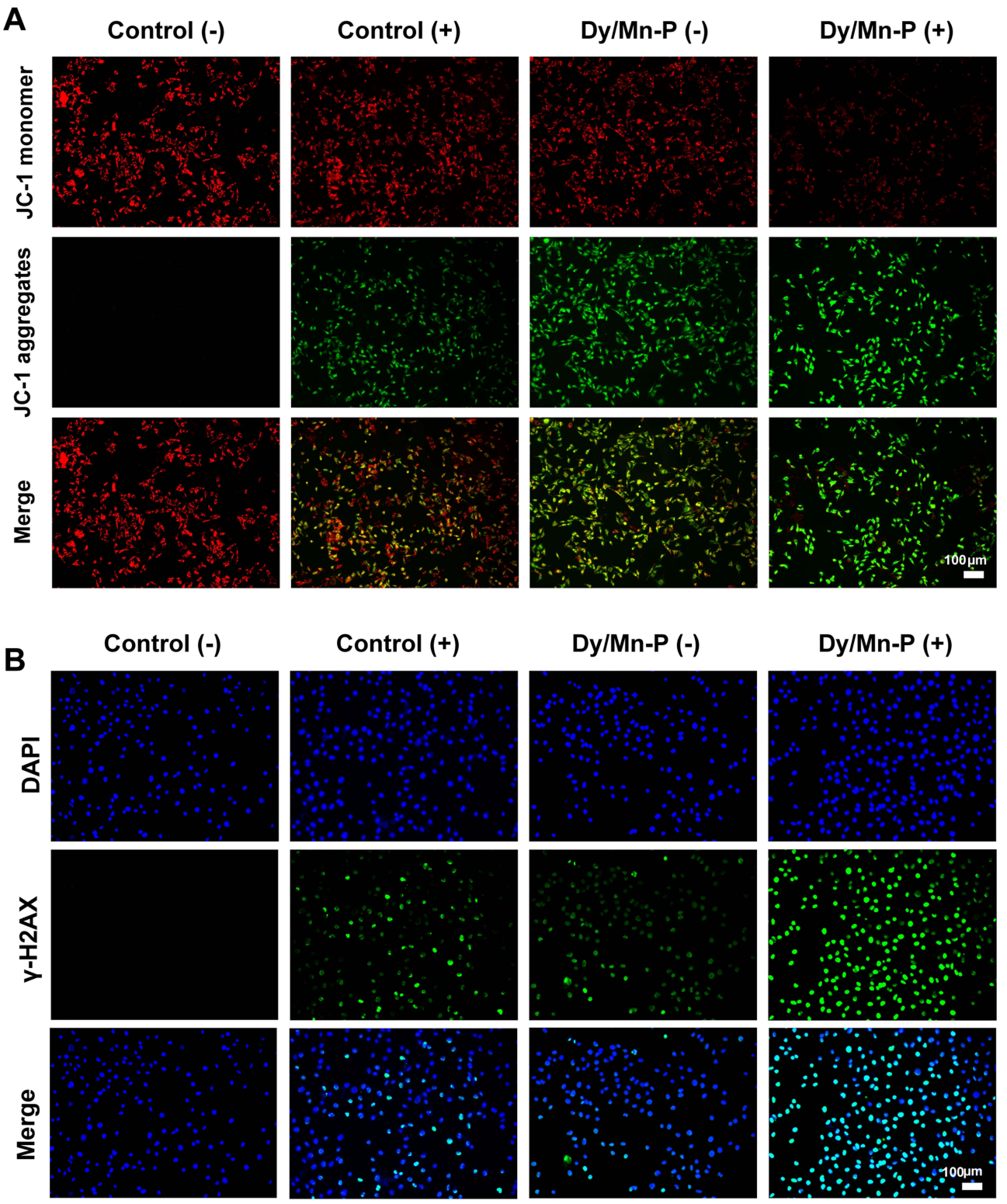

Figure 5 Mitochondrial membrane potential changes and DNA damage. (**A**) JC-1 staining for detecting the change of mitochondrial membrane potential in B16-F10 cells after indicated treatments. Scale bar = 100 μm. (**B**) Immunofluorescence images of γ-H2AX foci. Scale bar = 100 μm.

pathway resulting in the secretion of IFN-β to promote DCs mature and pro-inflammatory cytokines release. Therefore, this research provides a novel approach for the development of radiosensitizers, ROS amplifiers, and STING pathway activation based on Dy/Mn-P NPs, and provides scientific theoretical support and guidance for high atomic numbers

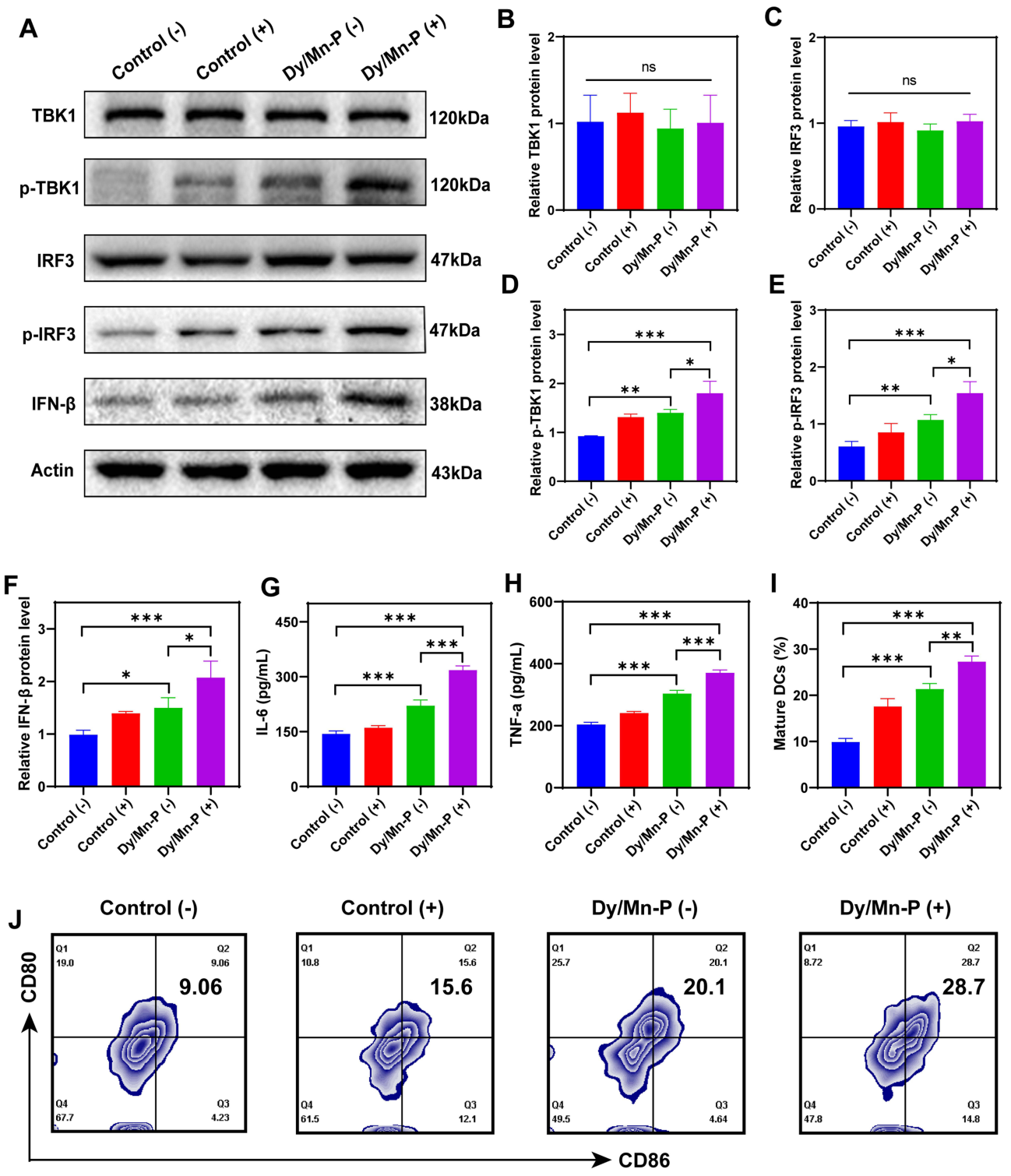

Figure 6 The activation of the STING pathway. (**A**) The Western blotting analysis protein expression in co-cultured cells, including IFN-β, TBK1, p-TBK1, IRF3, and p-IRF3 protein. (**B-F**) Quantitative analysis of IFN-β, TBK1, p-TBK1, IRF3, and p-IRF3 protein by Western blot. Data were presented as mean ± SD (n = 3). (**G** and **H**) The secretion of IL-6 and TNF-a in cell supernatant. Data were presented as mean ± SD (n = 3). (**I** and **J**) Representative flow cytometry plots (**J**) and quantification (**I**) of mature DCs ($CD80^+CD86^+$) via STING activation evaluated by flow cytometry (n = 3). Statistical significance was calculated via one-way ANOVA with Tukey's test: $^*P < 0.05$; $^{**}P < 0.01$; $^{***}P < 0.001$.

combined manganese ion complexes in further clinical application. This work not only sheds light on a ROS amplifier based on Dy/Mn-P for regulating radio-resistance caused by TME but also paves an avenue toward broadening the application of radiotherapy into immunotherapy.

Acknowledgments

The authors thank Guangdong Fine Chemical Research Institute and Shantou University for providing the experimental space and equipment.

Disclosure

The authors declare that they have no known competing financial interests or personal relationships that could have appeared to influence the work reported in this paper.

References

1. Knoll MA, Jagsi R, Rosenzweig K. Focal Radiation Therapy for Cancer. *JAMA Oncol*. 2019;5(3):442. doi:10.1001/jamaoncol.2018.5868
2. Parisi S, Ferini G, Lillo S, et al. Stereotactic boost on residual disease after external-beam irradiation in clinical stage III non-small cell lung cancer: mature results of stereotactic body radiation therapy post radiation therapy (SBRTpostRT) study. *Radiol Med*. 2023;128(7):877–885. doi:10.1007/s11547-023-01659-w
3. Siddique S, Chow JCL. Recent Advances in Functionalized Nanoparticles in Cancer Theranostics. *Nanomaterials*. 2022;12(16):2826. doi:10.3390/nano12162826
4. Ghaffarlou M, Mohammadi A, Mousazadeh N, et al. Facile preparation of silver based radiosensitizers via biomineralization method for enhanced in vivo breast cancer radiotherapy. *Sci Rep*. 2023;13(1):15131. doi:10.1038/s41598-023-40763-9
5. Rashidzadeh H, Seidi F, Ghaffarlou M, et al. Preparation of alginate coated Pt nanoparticle for radiosensitization of breast cancer tumor. *Int J Biol Macromol*. 2023;233:123273. doi:10.1016/j.ijbiomac.2023.123273
6. Liu N, Zhu J, Zhu W, et al. X-ray-Induced Release of Nitric Oxide from Hafnium-Based Nanoradiosensitizers for Enhanced Radio-Immunotherapy. *Adv Mater*. 2023;35(29).
7. Moloudi K, Khani A, Najafi M, et al. Critical parameters to translate gold nanoparticles as radiosensitizing agents into the clinic. *Wiley Int Rev Nanomed Nanobiotechnol*. 2023;15(6):e1886. doi:10.1002/wnan.1886
8. Zhou D, Gao Y, Yang Z, et al. Biomimetic Upconversion Nanoplatform Synergizes Photodynamic Therapy and Enhanced Radiotherapy against Tumor Metastasis. *ACS Appl Mater Interfaces*. 2023;15(22):26431–26441. doi:10.1021/acsami.3c03636
9. Fu W, Zhang X, Mei L, et al. Stimuli-Responsive Small-on-Large Nanoradiosensitizer for Enhanced Tumor Penetration and Radiotherapy Sensitization. *ACS Nano*. 2020;14(8):10001–10017. doi:10.1021/acsnano.0c03094
10. Gong T, Li Y, Lv B, et al. Full-Process Radiosensitization Based on Nanoscale Metal-Organic Frameworks. *ACS Nano*. 2020;14(3):3032–3040. doi:10.1021/acsnano.9b07898
11. Nosrati H, Salehiabar M, Charmi J, et al. Enhanced In Vivo Radiotherapy of Breast Cancer Using Gadolinium Oxide and Gold Hybrid Nanoparticles. *ACS Appl Bio Mater*. 2023;6(2):784–792. doi:10.1021/acsabm.2c00965
12. Santiago CA, Chow JCL. Variations in Gold Nanoparticle Size on DNA Damage: a Monte Carlo Study Based on a Multiple-Particle Model Using Electron Beams. *Appl Sci*. 2023;13(8):4916. doi:10.3390/app13084916
13. Cheng K, Sano M, Jenkins CH, et al. Synergistically Enhancing the Therapeutic Effect of Radiation Therapy with Radiation Activatable and Reactive Oxygen Species-Releasing Nanostructures. *ACS Nano*. 2018;12(5):4946–4958. doi:10.1021/acsnano.8b02038
14. Li N, Yu L, Wang J, et al. A mitochondria-targeted nanoradiosensitizer activating reactive oxygen species burst for enhanced radiation therapy. *Chem Sci*. 2018;9(12):3159–3164. doi:10.1039/C7SC04458E
15. Chow JCL, Ruda HE. Flash Radiotherapy: innovative Cancer Treatment. *Encyclopedia*. 2023;3(3):808–823. doi:10.3390/encyclopedia3030058
16. Siddique S, Ruda HE, Chow JCL. FLASH Radiotherapy and the Use of Radiation Dosimeters. *Cancers*. 2023;15(15):3883. doi:10.3390/cancers15153883
17. Chu ZY, Yang J, Zheng W, Sun JW, Wang WN, Qian HS. Recent advances on modulation of H2O2 in tumor microenvironment for enhanced cancer therapeutic efficacy. *Coord Chem Rev*. 2023;481.
18. Xu Q, Zhang Y, Yang Z, et al. Tumor microenvironment-activated single-atom platinum nanozyme with H(2)O(2) self-supplement and O(2)-evolving for tumor-specific cascade catalysis chemodynamic and chemoradiotherapy. *Theranostics*. 2022;12(11):5155–5171. doi:10.7150/thno.73039
19. Zhang H, Han R, Song P, et al. Hydrogen peroxide self-sufficient and glutathione-depleted nanoplatform for boosting chemodynamic therapy synergetic phototherapy. *J Colloid Interface Sci*. 2023;629(Pt A):103–113. doi:10.1016/j.jcis.2022.08.156
20. Ye MJ, Gao Y, Liang MY, et al. Microenvironment-responsive chemotherapeutic nanogels for enhancing tumor therapy via DNA damage and glutathione consumption. *Chin Chem Lett*. 2022;33(9):4197–4202. doi:10.1016/j.cclet.2022.01.086
21. Zhou Z, Guan B, Xia H, Zheng R, Xu B. Particle radiotherapy in the era of radioimmunotherapy. *Cancer Lett*. 2023;567:216268. doi:10.1016/j.canlet.2023.216268
22. Viswanath D, Park J, Misra R, et al. Nanotechnology-enhanced radiotherapy and the abscopal effect: current status and challenges of nanomaterial-based radio-immunotherapy. *Wiley Int Rev Nanomed Nanobiotechnol*;2023. e1924. doi:10.1002/wnan.1924
23. Song QX, Lan GD, Li Q, et al. A hydrogel-enabled cascade amplification of radiosensitization and immune activation for cancer radiotherapy. *Chem Eng J*. 2023;462.
24. Liu T, Pei P, Shen WH, Hu L, Yang K. Radiation-Induced Immunogenic Cell Death for Cancer Radioimmunotherapy. *Small Methods*. 2023.
25. Zhang X, Zhang H, Zhang J, et al. The paradoxical role of radiation-induced cGAS-STING signalling network in tumour immunity. *Immunology*. 2023;168(3):375–388. doi:10.1111/imm.13592
26. Kho VM, Mekers VE, Span PN, Bussink J, Adema GJ. Radiotherapy and cGAS/STING signaling: impact on MDSCs in the tumor microenvironment. *Cell Immunol*. 2021;362:104298. doi:10.1016/j.cellimm.2021.104298
27. Mathieu M, Budhu S, Nepali PR, et al. Activation of Sting in Response to Partial-Tumor Radiation Exposure. *Int J Radiat Oncol Biol Phys*. 2023;117(4):955–965. doi:10.1016/j.ijrobp.2023.05.032

28. Du SS, Chen GW, Yang P, et al. Radiation Therapy Promotes Hepatocellular Carcinoma Immune Cloaking via PD-L1 Upregulation Induced by cGAS-STING Activation. *Int J Radiat Oncol Biol Phys*. 2022;112(5):1243–1255. doi:10.1016/j.ijrobp.2021.12.162
29. Zheng SJ, Yang M, Luo JQ, et al. Manganese-Based Immunostimulatory Metal-Organic Framework Activates the cGAS-STING Pathway for Cancer Metalloimmunotherapy. *ACS Nano*. 2023;17(16):15905–15917. doi:10.1021/acsnano.3c03962
30. Cai L, Wang Y, Chen Y, et al. Manganese(ii) complexes stimulate antitumor immunity via aggravating DNA damage and activating the cGAS-STING pathway. *Chem Sci*. 2023;14(16):4375–4389. doi:10.1039/D2SC06036A
31. Lv M, Chen M, Zhang R, et al. Manganese is critical for antitumor immune responses via cGAS-STING and improves the efficacy of clinical immunotherapy. *Cell Res*. 2020;30(11):966–979. doi:10.1038/s41422-020-00395-4
32. Wang C, Guan Y, Lv M, et al. Manganese Increases the Sensitivity of the cGAS-STING Pathway for Double-Stranded DNA and Is Required for the Host Defense against DNA Viruses. *Immunity*. 2018;48(4):675–687 e677. doi:10.1016/j.immuni.2018.03.017
33. He H, Du L, Xue H, et al. Triple Tumor Microenvironment-Responsive Ferroptosis Pathways Induced by Manganese-Based Imageable Nanoenzymes for Enhanced Breast Cancer Theranostics. *Small Methods*. 2023;7(7):e2300230. doi:10.1002/smtd.202300230
34. Jia C, Guo Y, Wu FG. Chemodynamic Therapy via Fenton and Fenton-Like Nanomaterials: strategies and Recent Advances. *Small*. 2022;18(6):e2103868. doi:10.1002/smll.202103868
35. Duan J, Liao T, Xu X, Liu Y, Kuang Y, Li C. Metal-polyphenol nanodots loaded hollow MnO(2) nanoparticles with a "dynamic protection" property for enhanced cancer chemodynamic therapy. *J Colloid Interface Sci*. 2023;634:836–851. doi:10.1016/j.jcis.2022.12.088
36. Roy I, Krishnan S, Kabashin AV, Zavestovskaya IN, Prasad PN. Transforming Nuclear Medicine with Nanoradiopharmaceuticals. *ACS Nano*. 2022;16(4):5036–5061. doi:10.1021/acsnano.1c10550
37. Wang J, Li Z, Wang Z, et al. Nanomaterials for Combinational Radio–Immuno Oncotherapy. *Adv Funct Mater*. 2020;30(30):56.
38. Liu Q, Duo YH, Fu JY, et al. Nano-immunotherapy: unique mechanisms of nanomaterials in synergizing cancer immunotherapy. *Nano Today*. 2021;36:101023. doi:10.1016/j.nantod.2020.101023
39. Rahm M, Hoffmann R, Ashcroft NW. Atomic and Ionic Radii of Elements 1-96. *Chemistry*. 2016;22(41):14625–32. doi:10.1002/chem.201602949
40. Yang S, Dai L, Mao L, et al. Effect of sodium tripolyphosphate incorporation on physical, structural, morphological and stability characteristics of zein and gliadin nanoparticles. *Int J Biol Macromol*. 2019;136:653–660. doi:10.1016/j.ijbiomac.2019.06.052
41. Ferreira Tomaz A, Sobral de Carvalho SM, Cardoso Barbosa R, et al. Ionically Crosslinked Chitosan Membranes Used as Drug Carriers for Cancer Therapy Application. *Materials*. 2018;11(10):2051. doi:10.3390/ma11102051
42. Li B, Zhang Y, Fu L, et al. Surface passivation engineering strategy to fully-inorganic cubic CsPbI(3) perovskites for high-performance solar cells. *Nat Commun*. 2018;9(1):1076. doi:10.1038/s41467-018-03169-0
43. Kanna RR, Sakthipandi K, Kumar AS, et al. Synthesis of dysprosium/Mn–Cu ferrite binary nanocomposite: analysis of structural, morphological, dielectric, and optomagnetic properties. *Ceram. Int.* 2020;46(9):13695–13703. doi:10.1016/j.ceramint.2020.02.157
44. Salavati-Niasari M, Javidi J, Davar F. Sonochemical synthesis of Dy2(CO3)3 nanoparticles, Dy(OH)3 nanotubes and their conversion to Dy2O3 nanoparticles. *Ultrason Sonochem*. 2010;17(5):870–877. doi:10.1016/j.ultsonch.2010.02.013
45. Carulli F, He M, Cova F, Erroi A, Li L, Brovelli S. Silica-Encapsulated Perovskite Nanocrystals for X-ray-Activated Singlet Oxygen Production and Radiotherapy Application. *ACS Energy Lett*. 2023;8(4):1795–1802. doi:10.1021/acsenergylett.3c00234
46. Clement S, Chen WJ, Deng W, Goldys EM. X-ray radiation-induced and targeted photodynamic therapy with folic acid-conjugated biodegradable nanoconstructs. *Int j Nanomed*. 2018;13:3553–3570. doi:10.2147/IJN.S164967
47. Shi Y, Zhou M, Zhang Y, Wang Y, Cheng J. MRI-guided dual-responsive anti-tumor nanostructures for synergistic chemo-photothermal therapy and chemodynamic therapy. *Acta Biomater*. 2023;158:571–582. doi:10.1016/j.actbio.2022.12.053
48. Wang P, Liang C, Zhu J, et al. Manganese-Based Nanoplatform As Metal Ion-Enhanced ROS Generator for Combined Chemodynamic/Photodynamic Therapy. *ACS Appl Mater Interfaces*. 2019;11(44):41140–41147. doi:10.1021/acsami.9b16617
49. Xu J, Shi R, Chen G, et al. All-in-One Theranostic Nanomedicine with Ultrabright Second Near-Infrared Emission for Tumor-Modulated Bioimaging and Chemodynamic/Photodynamic Therapy. *ACS Nano*. 2020;14(8):9613–9625. doi:10.1021/acsnano.0c00082
50. He S, Cheng J, Sun L, et al. HMGB1 released by irradiated tumor cells promotes living tumor cell proliferation via paracrine effect. *Cell Death Dis*. 2018;9(6):648. doi:10.1038/s41419-018-0626-6
51. Huang Y, Jiang Y, Xiao Z, et al. Three birds with one stone: a ferric pyrophosphate based nanoagent for synergetic NIR-triggered photo/chemodynamic therapy with glutathione depletion. *Chem Eng J*. 2020;380.
52. Niu B, Liao K, Zhou Y, et al. Application of glutathione depletion in cancer therapy: enhanced ROS-based therapy, ferroptosis, and chemotherapy. *Biomaterials*. 2021;277:121110. doi:10.1016/j.biomaterials.2021.121110
53. Payen VL, Zampieri LX, Porporato PE, Sonveaux P. Pro- and antitumor effects of mitochondrial reactive oxygen species. *Cancer Metastasis Rev*. 2019;38(1–2):189–203. doi:10.1007/s10555-019-09789-2
54. Hao W, Zhao C, Li G, et al. Blue LED light induces cytotoxicity via ROS production and mitochondrial damage in bovine subcutaneous preadipocytes. *Environ Pollut*. 2023;322:121195. doi:10.1016/j.envpol.2023.121195
55. Widjaja L, Werner RA, Krischke E, et al. Individual radiosensitivity reflected by gamma-H2AX and 53BP1 foci predicts outcome in PSMA-targeted radioligand therapy. *Eur J Nucl Med Mol Imaging*. 2023;50(2):602–612. doi:10.1007/s00259-022-05974-8
56. Huang D, Wu T, Lan S, Liu C, Guo Z, Zhang W. In situ photothermal nano-vaccine based on tumor cell membrane-coated black phosphorus-Au for photo-immunotherapy of metastatic breast tumors. *Biomaterials*. 2022;289:121808. doi:10.1016/j.biomaterials.2022.121808